

# Virtual monoenergetic imaging in rapid kVp-switching dual-energy CT (DECT) of the abdomen: impact on CT texture analysis

Vinit Baliyan,<sup>1</sup> Hamed Kordbacheh,<sup>1</sup> Bimal Parameswaran,<sup>2</sup> Balaji Ganeshan,<sup>3</sup>  
Dushyant Sahani,<sup>1</sup> Avinash Kambadakone<sup>1</sup>

<sup>1</sup>Department of Radiology, Massachusetts General Hospital, White 270, 55 Fruit Street, Boston, MA 02114, USA

<sup>2</sup>Imaging Associates, Eastern Health, Box Hill, VIC, Australia

<sup>3</sup>Institute of Nuclear Medicine, University College London, London, UK

## Abstract

**Purpose:** To study the impact of keV levels of virtual monoenergetic images generated from rapid kVp-switching dual-energy CT (rsDECT) on CT texture analysis (CTTA).

**Methods:** This study included 30 consecutive patients ( $59.3 \pm 12$  years; range 34–77 years; 17M:13F) who underwent portal venous phase abdominal CT on a rsDECT scanner. Axial 5-mm monoenergetic images at 5 energy levels (40/50/60/70/80 keV) were created and CTTA of liver was performed. CTTA comprised a filtration-histogram technique with different spatial scale filter (SSF) values (0–6). CTTA quantification at each SSF value included histogram-based statistical parameters such as mean intensity, standard deviation (SD), entropy, mean of positive pixels (MPP), skewness, and kurtosis. The values were compared using repeated measures ANOVA.

**Results:** Among the different CTTA metrics, mean intensity (at SSF > 0), skewness, and kurtosis did not show variability whereas entropy, MPP, and SD varied with different keV levels. There was no change in skewness and kurtosis values for all 6 filters ( $p > 0.05$ ). Mean intensity showed no change for filters 2–6 ( $p > 0.05$ ). Mean intensity at SSF = 0 i.e., mean attenuations were  $91.2 \pm 2.9$ ,  $108.7 \pm 3.6$ ,  $136.1 \pm 4.7$ ,  $179.8 \pm 6.9$ , and  $250.5 \pm 10.1$  HU for 80, 70, 60, 50, and 40 keV images, respectively demonstrating significant variability (decrease) with increasing keV levels ( $p < 0.001$ ). Entropy, MPP, and SD values showed a statistically significant decrease with increasing keV of

monoenergetic images on all 6 filters ( $p < 0.001$ ).

**Conclusion:** The energy levels of monoenergetic images have variable impact on the different CTTA parameters, with no significant change in skewness, kurtosis, and filtered mean intensity whereas significant decrease in mean attenuation, entropy, MPP, and SD values with increasing energy levels.

**Key words:** Dual energy CT—CT texture analysis—Virtual monoenergetic imaging

Tissue heterogeneity is an important histological feature of malignant tumors [1]. One of the components of tissue heterogeneity is vascular variation which contributes to adverse tumor microenvironment and regional tumor hypoxia. Vascular heterogeneity leads to aggressive tumor biology facilitating increased risk of local invasion and systemic metastasis, impaired delivery of systemic chemotherapeutic agents, and cellular resistance to chemotherapy [1]. Imaging surrogates of tissue heterogeneity (especially vascular) on cross-sectional radiological techniques such as CT and MRI include variable lesion attenuation/intensity and enhancement characteristics. Texture analysis is a method of quantifying the lesion heterogeneity on medical images (CT and MRI) and is emerging as a potentially useful tool for assessing prognosis and treatment response in cancer imaging [2, 3]. CT-based texture parameters obtained from tumors have been shown to correlate with histological features, and in comparison to histological analysis it is less invasive and easier to perform [3]. CT texture analysis (CTTA) has been shown to be useful in detection [4–9], characterization [10–14], staging, and prognostication of

various malignancies [15–22]. CTTA has been shown to be a marker for tumor metabolism, angiogenesis, key molecular marker expression, and patient survival in lung and gastrointestinal cancers [15–23]. Texture analysis performed using CT and MRI has also emerged as a tool for therapeutic response assessment. CTTA has been reported to be predictive biomarker for response to tyrosine kinase inhibitors in metastatic renal cell cancer [24], and chemotherapy in primary and metastatic colorectal cancer [25–27], non-small cell lung cancer [28], esophageal cancer [29], and soft tissue sarcoma [30]. MRI image texture analysis has also been found to be a predictor of chemotherapeutic response in breast cancer [31–34].

Dual-energy CT (DECT) allows simultaneous image acquisition at two different energies which leads to generation of material/energy specific attenuation information and a wide range of CT image datasets. Rapid kVp-switching (rsDECT) is a type of source-based DECT in which the single X-ray source rapidly switches between low and high tube voltages to generate near-simultaneous dual-energy projections. Virtual monoenergetic images are post-processed DECT images that provide projected attenuation maps equivalent to an actual acquisition at monochromatic X-ray beam of specific photon energy (40–190 keV) [35, 36]. Generally, most of the DECT protocols generate arterial phase monochromatic images at 50–60 keV and portal venous phase images at 60–75 keV as they provide the most optimal balance between improved SNR and image noise [37]. Monoenergetic images demonstrate variations in attenuation values (HU) based on the energy level of reconstruction [38]. Similarly, corresponding pixels from various monoenergetic and material decomposition images differ in attenuation depending on the material composition. As texture analysis is based on mathematical description of pixel gray-level intensity information, DECT post-processing might have an impact on image texture analysis. Increasing use of DECT for routine clinical and research purposes means that CTTA would be increasingly applied on post-processed DECT datasets and understanding their interplay is imperative for precise interpretation of research findings and standardization of imaging protocols. The impact of various energy levels of monoenergetic images on CTTA has not been studied before. Therefore, we undertook this research with the purpose of studying the impact of the energy level (keV) of reconstructed virtual monoenergetic images generated from rapid kVp-switching dual-energy CT on CTTA parameters.

## Materials and methods

### Patient population

This study was IRB approved and HIPAA compliant. The retrospective study included 30 consecutive patients (age  $59.3 \pm 12$  years; range 34–77 years; 17M:13F, BMI

$28.5 \pm 7$ ) who underwent portal venous phase abdominal CT for oncologic work-up. The patients included in the cohort did not have documented liver disease such as hepatitis, cirrhosis, or hepatic steatosis in the medical record. Careful evaluation of the CT scans in these patients revealed no evidence of focal liver lesions such as metastases/cysts. The hepatic parenchymal enhancement in these patients was homogeneous without evidence of diffuse liver disease such as hepatic steatosis or cirrhosis. A liver–spleen attenuation difference of  $-25$  HU on the portal venous phase exam was taken as the criteria for hepatic steatosis. The liver function tests were within normal limits. All the patients included in the study were treatment naïve without evidence of systemic or locoregional therapies such as ablation or transarterial chemoembolization.

### Imaging technique

All the patients included in the study had undergone a portal venous phase abdominal CT exam on a single source rapid kVp-switching DECT scanner (GE Discovery CT 750 HD scanner, GE Healthcare, Milwaukee, WI, USA) in the DE mode (See Table 1 for CT protocol). Portal venous phase images were obtained 70 s following intravenous administration of 80–90 mL of iodinated contrast material (Iovue, 370 mgI/mL, Bracco Diagnostics, Princeton, NJ, USA) at an injection rate of 3 mL/s. The DECT image datasets were transferred from PACS to a dedicated post-processing workstation for creation of the monoenergetic images. Axial virtual monoenergetic images of 5-mm thickness were reconstructed on advantage 4.6 workstation at 5 different energy levels (40, 50, 60, 70, and 80 keV). From the post-processed monoenergetic image datasets, one single axial image at the level of porta hepatis was selected for CTTA analysis. A total of 150 axial CT images (30 DECT

**Table 1.** Scan parameters

Parameters	ssDECT	
Tube potential (kVp)	80 kV/140 kV	
GSI parameters for patients under 150 lbs	GSI	23
	CTDI	11.32
	mA (fixed)	375
	Rotation time	0.7 s
	Pitch	1.375
	Collimation	$64 \times 0.625$
	Speed	55 mm/s
GSI parameters for patients 151–250 lbs	GSI	3
	CTDI	13.33
	mA (fixed)	630
	Rotation time	1 s
	Pitch	0.984
	Collimation	$64 \times 0.625$
	Speed	39.37 mm/s
Slice thickness/interval	5 mm/5 mm	
Iterative reconstruction	ASIR (50%)	

scans  $\times$  5 different keV levels) constituted the final dataset for CTTA analysis.

### *CT texture analysis*

The selected DICOM images were saved and uploaded to commercially available research software TexRAD (TexRAD Ltd [www.texrad.com](http://www.texrad.com) part of Feedback Plc, Cambridge, UK) for image texture/heterogeneity assessment. This software has been extensively reported and validated for various oncologic applications [2, 15–17, 19, 23, 39, 40]. CTTA of the different monoenergetic image datasets were performed by placing regions of interest (ROIs) on the liver at corresponding locations on monoenergetic images of different keV levels. Large rectangular ROIs (3–5 cm<sup>2</sup>) were placed at the homogeneously enhancing liver parenchyma at the sub-capsular location devoid of vessels.

CTTA algorithm for liver employs a thresholding procedure that excludes any pixels corresponding to areas of fat, air, and bright vessels with attenuation values outside the range of 0–300 HU. CTTA comprised a filtration-histogram technique where the filtration step/technique produced a series of derived images extracting and enhancing objects/features of varying intensities and sizes corresponding to different spatial scale filter (SSF) values corresponding to fine (SSF = 2, features of 2 mm in radius), medium (SSF = 3, 4, 5, features of 3, 4 or 5 mm), and coarse (SSF = 6, features of 6 mm in radius) texture scales. Fine texture may represent parenchymal/tissue features; while medium/coarse texture may reflect larger vascular components, both representing different but biologically important information. As the CT scanner pixel resolution tends to be sub-mm voxel so any features less than twice the pixel resolution will most likely be reflecting photon noise hence SSF values less than 2 mm were not considered. Filtration was followed by heterogeneity quantification using mean intensity (average brightness), SD (standard deviation; width of the distribution), mean value of positive pixels (MPP; the average value of all the pixels with positive value; represents location of distribution), entropy (a measure of irregularity or complexity), skewness (a measure of asymmetry of the histogram), and kurtosis (a measure of peakedness or pointedness or sharpness of the distribution). In addition, these histogram parameters were also quantified from the conventional CT image without filtration (i.e., SSF = 0). CTTA parameters included mean, standard deviation (SD), entropy, mean of positive pixels (MPP), skewness, and kurtosis at 6 different SSF values (0, 2, 3, 4, 5, and 6). A recent article [40] highlights filtration-histogram-based CTTA and describes how various texture parameters reflect different components of visual image (heterogeneity) features such as number of objects/features, size of objects/features, and variation in intensity

of these objects/features in relation to the background of the tissue within the ROI (Fig. 1).

### *Statistical analysis*

Statistical analyses were carried out using the MedCalc software version 17.6 (Ostend Belgium). The mean attenuation values (HU which is mean intensity values at SSF = 0) and textural parameters (mean intensity, SD, entropy, MPP, skewness, and kurtosis at different SSF values) from the different monoenergetic images were compared using repeated measures using ANOVA. For all comparisons,  $p < 0.05$  was considered to indicate a statistically significant difference.

## **Results**

### *CT attenuation and monoenergetic image keV level*

The mean attenuation of the liver parenchyma showed an increasing trend with decreasing keV level of the monoenergetic images. The mean attenuation was  $91.2 \pm 2.9$ ,  $108.7 \pm 3.6$ ,  $136.1 \pm 4.7$ ,  $179.8 \pm 6.9$ , and  $250.5 \pm 10.1$  HU for 80, 70, 60, 50, and 40 keV images, respectively ( $p < 0.001$ ).

### *CTTA variables and monoenergetic image keV level*

Among the different CTTA parameters measured at different monoenergetic levels, kurtosis, skewness, and filtered mean intensity showed least variability (more robust parameters) compared to entropy, SD, and MPP. There was no significant change in the kurtosis values along the energy levels of the monoenergetic images for most comparisons across all 6 filters ( $p > 0.1$ ) (Table 2). The filtered mean intensity showed no significant change with varying energy levels of monoenergetic images for all filters ( $p > 0.05$ ) (Table 3). There was no significant change in the skewness values at different keV levels for unfiltered images (SSF = 0) and for fine (SSF = 2) and coarse (SSF = 6) filters (Table 4). The skewness values showed a significant decreasing trend with increasing keV values at medium size filters (SSF = 3, 4, & 5) (Table 4). But there was no significant difference for most subset comparisons on post hoc analysis (Table 4). The entropy, MPP, and SD values showed a statistically significant decrease with increasing keV of monoenergetic images on all 6 filters ( $p < 0.001$ ; for all parameters), except for few individual subset comparisons on post hoc analysis (Tables 5, 6, 7).

## **Discussion**

CT texture analysis which uses mathematical descriptors to describe the distribution of pixel intensity values

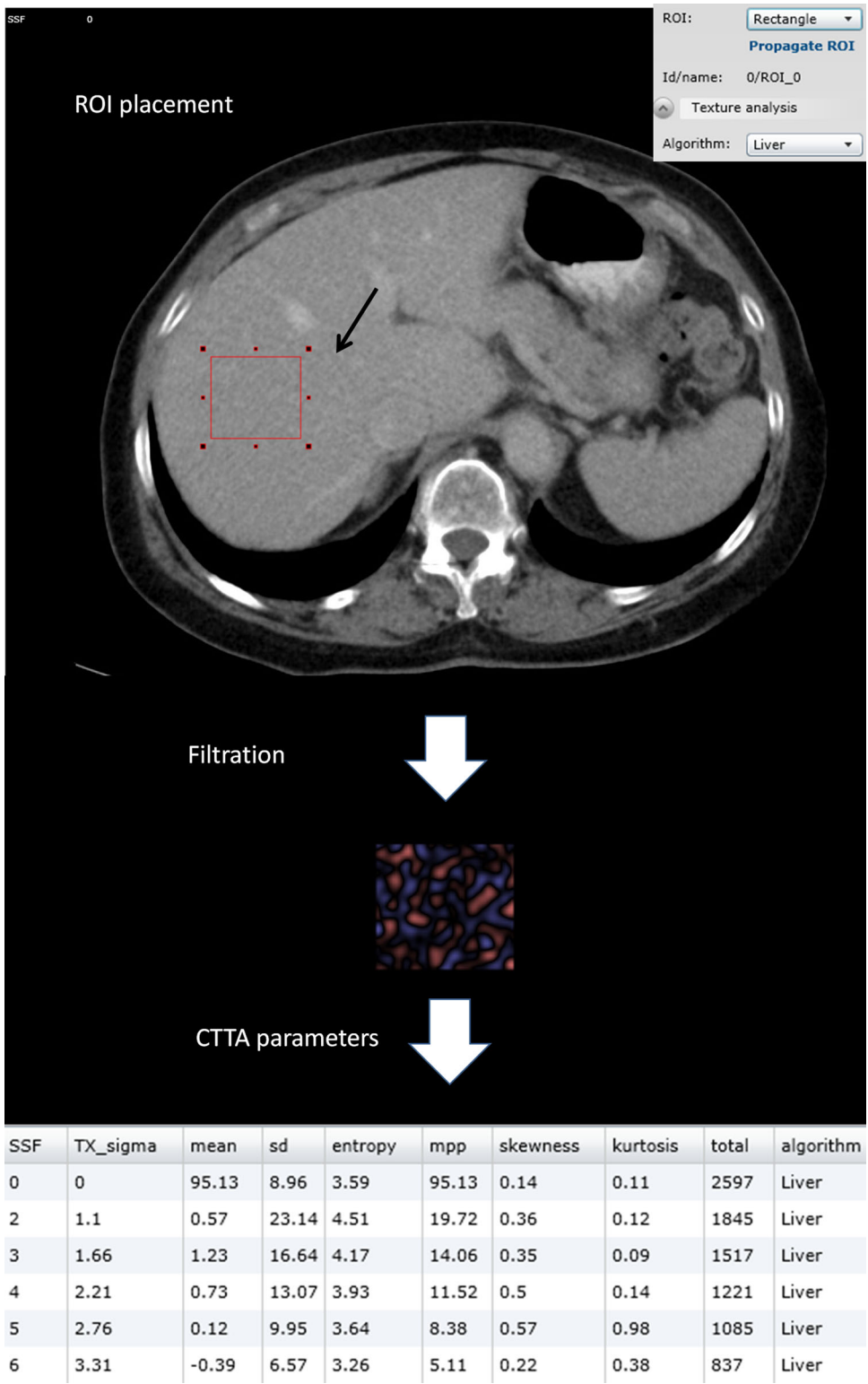


Fig. 1. Illustration showing CTTA process. Large rectangular ROIs (arrow) were placed at the homogeneously enhancing liver parenchyma devoid of vessels. CTTA comprised a filtration-histogram technique where the filtration step/technique produced a series of derived images extracting and enhancing objects/features of varying intensities and sizes corresponding to different spatial scale filter (SSF) values including 0, 2, 3, 4, 5, and 6. The CTTA parameters of image were derived for each value of SSF.

within a ROI and therefore provide a marker for tumor biology has attracted a lot of recent interest in oncology research. In addition to its established applications of lung nodule characterization and detection of colonic polyps, its role as a biomarker for assessment and prediction of treatment response to various therapies is

emerging [4–14, 24–29, 31–34]. Rising use of CTTA in oncological imaging has been paralleled by the increasing performance of DECT in routine clinical and research practice across multiple centers. As the spectrum of the DECT datasets, particularly monoenergetic images are being investigated for their role in improving imaging

**Table 2.** Kurtosis values with different filters (SSF) at different keV

SSF	Kurtosis (mean $\pm$ SD)						Post-ANOVA
	40 keV	50 keV	60 keV	70 keV	80 keV	<i>p</i> value	
0	0.49 $\pm$ 0.17	1.61 $\pm$ 1.3	0.18 $\pm$ 0.04	0.24 $\pm$ 0.08	- 0.002 $\pm$ 0.02	0.1082	Significant difference between 60 & 80 keV and between 70 & 80 keV. Rest of the comparisons were not different.
2	0.18 $\pm$ 0.10	0.15 $\pm$ 0.11	0.22 $\pm$ 0.14	0.34 $\pm$ 0.16	- 0.09 $\pm$ 0.06	0.1231	No significant difference on subset comparisons.
3	0.09 $\pm$ 0.15	0.14 $\pm$ 0.15	0.22 $\pm$ 0.20	0.19 $\pm$ 0.16	- 0.22 $\pm$ 0.07	0.1393	No significant difference on subset comparisons.
4	0.01 $\pm$ 0.13	0.003 $\pm$ 0.13	0.07 $\pm$ 0.16	0.03 $\pm$ 0.13	- 0.32 $\pm$ 0.09	0.1027	No significant difference on subset comparisons.
5	- 0.24 $\pm$ 0.11	- 0.16 $\pm$ 0.12	- 0.20 $\pm$ 0.16	- 0.17 $\pm$ 0.14	- 0.35 $\pm$ 0.13	0.5449	No significant difference on subset comparisons.
6	- 0.50 $\pm$ 0.10	- 0.49 $\pm$ 0.09	- 0.36 $\pm$ 0.15	- 0.44 $\pm$ 0.12	- 0.57 $\pm$ 0.16	0.7961	No significant difference on subset comparisons.

**Table 3.** Mean intensity values with different filters (SSF) at different keV

SSF	Parameter "Mean" (mean $\pm$ SD)						Post-ANOVA
	40 keV	50 keV	60 keV	70 keV	80 keV	<i>p</i> value	
0 (attenuation)	250.5 $\pm$ 10.1	179.8 $\pm$ 6.9	136.1 $\pm$ 4.7	108.7 $\pm$ 3.6	91.2 $\pm$ 2.9	< 0.0001	All subset comparisons were significantly different.
2	0.73 $\pm$ 0.78	0.64 $\pm$ 0.32	- 0.05 $\pm$ 0.31	0.25 $\pm$ 0.16	- 0.008 $\pm$ 0.18	0.298	No significant difference on subset comparisons.
3	1.56 $\pm$ 1.02	0.99 $\pm$ 0.45	0.21 $\pm$ 0.55	0.02 $\pm$ 0.28	0.03 $\pm$ 0.34	0.0856	No significant difference on subset comparisons.
4	0.52 $\pm$ 1.3	0.43 $\pm$ 1.02	0.95 $\pm$ 0.69	- 0.18 $\pm$ 0.68	0.17 $\pm$ 0.58	0.6157	No significant difference on subset comparisons.
5	1 $\pm$ 1.9	- 0.02 $\pm$ 1.3	1.4 $\pm$ 0.98	0.37 $\pm$ 1.06	0.77 $\pm$ 0.89	0.9883	No significant difference on subset comparisons.
6	1.02 $\pm$ 2.62	0.3 $\pm$ 1.8	2.21 $\pm$ 1.39	1.32 $\pm$ 1.38	1.16 $\pm$ 1.12	0.8071	No significant difference on subset comparisons.

**Table 4.** Skewness values with different filters (SSF) at different keV

SSF	Skewness (mean $\pm$ SD)						Post-ANOVA
	40 keV	50 keV	60 keV	70 keV	80 keV	<i>p</i> value	
0	0.008 $\pm$ 0.06	- 0.06 $\pm$ 0.13	0.1 $\pm$ 0.02	0.1 $\pm$ 0.03	0.03 $\pm$ 0.02	0.2018	No significant difference on subset comparisons.
2	0.11 $\pm$ 0.04	0.10 $\pm$ 0.04	0.14 $\pm$ 0.05	0.14 $\pm$ 0.05	0.04 $\pm$ 0.03	0.4362	No significant difference on subset comparisons.
3	0.22 $\pm$ 0.07	0.19 $\pm$ 0.06	0.18 $\pm$ 0.07	0.22 $\pm$ 0.07	- 0.007 $\pm$ 0.04	< 0.05	Only 40 & 80 keV were significantly different.
4	0.28 $\pm$ 0.08	0.25 $\pm$ 0.08	0.19 $\pm$ 0.08	0.20 $\pm$ 0.08	- 0.01 $\pm$ 0.05	< 0.05	Only 40 & 80 keV were significantly different.
5	0.21 $\pm$ 0.09	0.26 $\pm$ 0.09	0.22 $\pm$ 0.08	0.16 $\pm$ 0.09	- 0.04 $\pm$ 0.08	< 0.05	No significant difference on subset comparisons.
6	0.017 $\pm$ 0.1	0.08 $\pm$ 0.09	0.06 $\pm$ 0.1	0.02 $\pm$ 0.1	- 0.06 $\pm$ 0.11	0.4969	No significant difference on subset comparisons.

diagnosis, it is crucial to understand their interplay with CTTA analysis.

Post-processed DECT images have been shown to affect attenuation measurements depending on the material composition [35, 36]. We found that certain CTTA parameters demonstrate less variability (more robust) compared to others at different energy levels of

monoenergetic images. There was no significant change in the kurtosis, skewness (showed no change at unfiltered images and with fine and coarse filters), and filtered mean intensity values along the different monoenergetic energy levels. Gaussian filter has a smoothing effect on the images and is probably mitigating the effects of dual-energy post-processing and hence the differences in

**Table 5.** Entropy values with different filters (SSF) at different keV

SSF	Entropy (mean $\pm$ SD)						Post-ANOVA
	40 keV	50 keV	60 keV	70 keV	80 keV	<i>p</i> value	
0	4.6 $\pm$ 0.05	4.3 $\pm$ 0.04	4.03 $\pm$ 0.05	3.7 $\pm$ 0.05	3.6 $\pm$ 0.04	< 0.0001	All subset comparisons were significantly different.
2	5.3 $\pm$ 0.05	5.08 $\pm$ 0.04	4.8 $\pm$ 0.04	4.5 $\pm$ 0.04	4.5 $\pm$ 0.04	< 0.0001	No difference between 70 & 80 keV. Rest of the subset comparisons were significantly different.
3	4.9 $\pm$ 0.06	4.7 $\pm$ 0.04	4.5 $\pm$ 0.05	4.2 $\pm$ 0.05	4.2 $\pm$ 0.05	< 0.0001	No difference between 70 & 80 keV. Rest of the subset comparisons were significantly different.
4	4.5 $\pm$ 0.1	4.4 $\pm$ 0.06	4.2 $\pm$ 0.06	3.9 $\pm$ 0.05	3.8 $\pm$ 0.06	< 0.0001	No difference between 40 & 50 keV, between 40 & 60 keV and between 70 & 80 keV. Rest of the subset comparisons were significantly different.
5	4.5 $\pm$ 0.07	4.1 $\pm$ 0.07	3.9 $\pm$ 0.1	3.7 $\pm$ 0.07	3.5 $\pm$ 0.09	< 0.0001	No difference between 70 & 80 keV. Rest of the subset comparisons were significantly different.
6	4.1 $\pm$ 0.11	3.8 $\pm$ 0.1	3.5 $\pm$ 0.14	3.3 $\pm$ 0.12	3.1 $\pm$ 0.15	< 0.0001	No difference between 60 & 70 keV and between 70 & 80 keV. Rest of the subset comparisons were significantly different.

**Table 6.** MPP values with different filters (SSF) at different keV

SSF	MPP (mean $\pm$ SD)						Post-ANOVA
	40 keV	50 keV	60 keV	70 keV	80 keV	<i>p</i> value	
0	250.5 $\pm$ 10.1	179.8 $\pm$ 6.9	136.1 $\pm$ 4.7	108.7 $\pm$ 3.6	91.2 $\pm$ 2.9	< 0.0001	All subset comparisons were significantly different.
2	57.2 $\pm$ 2.4	40.3 $\pm$ 1.7	31.4 $\pm$ 1.5	22.6 $\pm$ 1.07	22.1 $\pm$ 1.005	< 0.0001	No difference between 70 & 80 keV. Rest of the subset comparisons were significantly different.
3	41.6 $\pm$ 2.2	29.03 $\pm$ 1.3	23.8 $\pm$ 1.3	17.09 $\pm$ 0.89	15.9 $\pm$ 0.78	< 0.0001	No difference between 70 & 80 keV. Rest of the subset comparisons were significantly different.
4	33.2 $\pm$ 2.8	22.8 $\pm$ 1.2	19.4 $\pm$ 1.2	13.5 $\pm$ 0.75	12.1 $\pm$ 0.73	< 0.0001	No difference between 70 & 80 keV. Rest of the subset comparisons were significantly different.
5	29.04 $\pm$ 2.8	19.09 $\pm$ 1.5	16.09 $\pm$ 1.5	11.4 $\pm$ 0.96	10.4 $\pm$ 0.95	< 0.0001	No difference between 70 & 80 keV. Rest of the subset comparisons were significantly different.
6	24.02 $\pm$ 2.8	15.2 $\pm$ 2.8	13.4 $\pm$ 1.7	9.7 $\pm$ 1.2	8.6 $\pm$ 1.1	< 0.0001	No difference between 50 & 60 keV and between 70 & 80 keV. Rest of the subset comparisons were significantly different.

**Table 7.** SD values with different filters (SSF) at different keV

SSF	SD (mean $\pm$ SD)						Post-ANOVA
	40 keV	50 keV	60 keV	70 keV	80 keV	<i>p</i> value	
0	29.1 $\pm$ 1.4	20.4 $\pm$ 0.9	15.07 $\pm$ 0.8	11.2 $\pm$ 0.5	10.3 $\pm$ 0.4	< 0.0001	All subset comparisons were significantly different.
2	71.03 $\pm$ 3.2	50.1 $\pm$ 2.2	38.8 $\pm$ 1.8	28.3 $\pm$ 1.3	27.4 $\pm$ 1.2	< 0.0001	No difference between 50 & 60 keV and between 70 & 80 keV. Rest of the subset comparisons were significantly different.
3	50.3 $\pm$ 2.7	35.2 $\pm$ 1.7	29.2 $\pm$ 1.6	20.7 $\pm$ 1.1	19.5 $\pm$ 0.9	< 0.0001	No difference between 70 & 80 keV. Rest of the subset comparisons were significantly different.
4	38.5 $\pm$ 3.1	27.05 $\pm$ 1.6	23.1 $\pm$ 1.5	16.3 $\pm$ 0.9	14.9 $\pm$ 0.9	< 0.0001	All subset comparisons were significantly different.
5	33.5 $\pm$ 2.6	22.2 $\pm$ 1.6	18.2 $\pm$ 1.6	13.2 $\pm$ 0.8	11.8 $\pm$ 1.1	< 0.0001	No difference between 70 & 80 keV. Rest of the subset comparisons were significantly different.
6	26.5 $\pm$ 2.5	17.3 $\pm$ 1.6	13.8 $\pm$ 1.5	10.1 $\pm$ 0.9	9.05 $\pm$ 1.1	< 0.0001	No difference between 70 & 80 keV. Rest of the subset comparisons were significantly different.

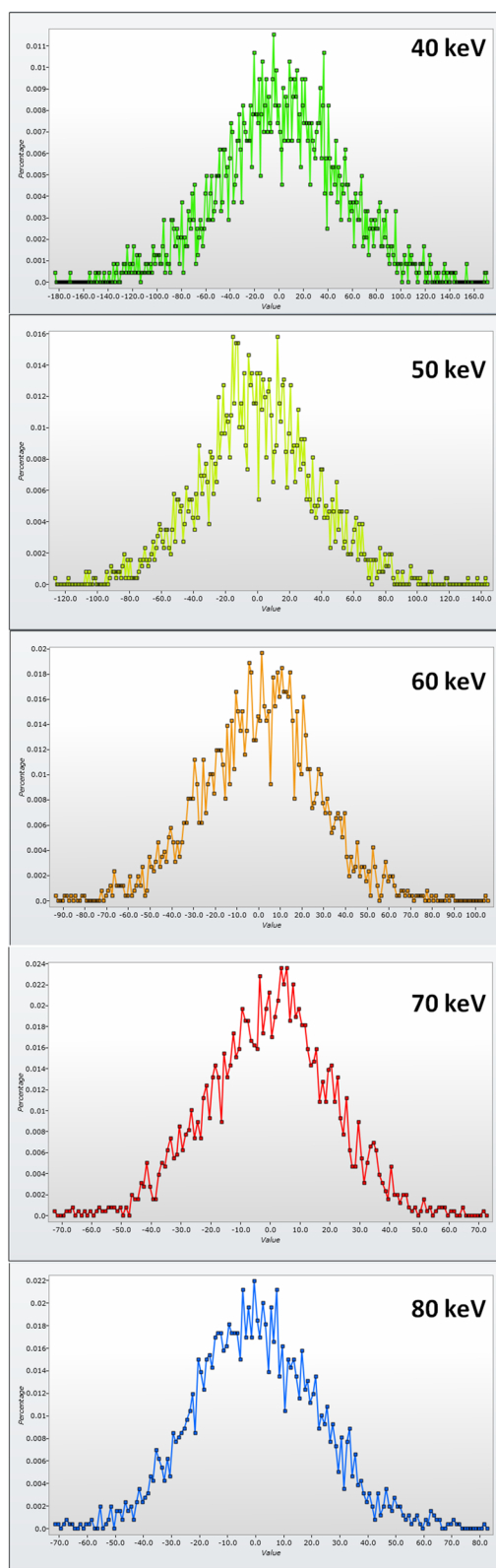


**Fig. 2.** Illustration showing the histogram plots of 40–80 keV images with fine filter (SSF 2). There is difference in standard deviation (as demonstrated by the range on x-axis); however, there is no difference in the shape/peakedness of the curve (kurtosis) and skewness.

attenuation/mean on unfiltered images is not reproduced on filtered images. Skewness represents the measure of asymmetry of texture histogram and this value could be positive or negative. A negative skew indicates a longer tail on the left side of the histogram, while a positive skew designates that the tail on the right side is longer than the left side. A zero value specifies uniform distribution of values on either side of the mean. The dual-energy post-processing did not have any impact on skewness in a homogeneously enhancing liver parenchyma. It probably can be explained by the fact that although the change in keV results in change in pixel intensity but this change is proportionate in all pixels and does not change their distribution around the mean (Fig. 2). Kurtosis is a measure of the peakedness of the histogram and this value could be positive or negative. A positive kurtosis indicates a histogram that is more peaked than a Gaussian (normal) distribution, while a negative kurtosis indicates a histogram that is flatter. The relative stability of kurtosis can also probably be explained by the proportionate impact on all pixels that did not change the distribution of pixel intensities around the mean (Fig. 2). The entropy, MPP, SD values across all filter levels and skewness (medium filter scale) showed a statistically significant decrease with increasing keV of monoenergetic images.

The findings of our study have two key implications. First, all the results of the prior studies on CTTA with polychromatic CT should be applied with care to the future studies on DECT monoenergetic images. Texture parameters are quantitative entities and certain parameters are less prone to variations due to DECT image specifications rather than actual pathological process. Second and more importantly, there has been an increase in the utilization of CTTA for the response assessment in various malignancies [24–30] with a simultaneous increase in the performance of DECT for oncological applications [41–45]. Thus, it is important to be aware of the impact of DECT post-processing on image texture to ensure the comparability of imaging studies acquired at different time points. Our study has demonstrated that some of the texture parameters such as kurtosis, filtered mean intensity values, and skewness values of unfiltered images and filtered images with fine and coarse filters do not change with changing keV and hence might be more reliable and robust compared to other quantifiers between different keV datasets. The quantifiers that demonstrate variability between different keV could benefit from some additional normalization techniques e.g., texture ratios at two filter (SSF) values [46–48] that have been shown to exhibit least variability with CT acquisition parameters—tube currents and tube voltages and predict patient survival in metastatic colorectal cancer study. Other normalization techniques could include dividing tissue texture of interest by muscle/water texture. These approaches could make the quantifiers

more reliable and robust and therefore applicable to DECT monoenergetic images. The implication of our study for clinical use and patient care translates to identification of CTTA parameters (e.g., kurtosis, skewness, and filtered mean) which are less variant (more robust) to variations in energy levels of monoenergetic images making them suitable for use in DECT applications.

Our study has few limitations. First, our sample size was small. Second, the measurements were performed on normal liver parenchyma and no measurements were made on actual focal lesions [46–48]. However, since our intent was to identify variations in CTTA with monoenergetic images, we relied on using normal parenchyma of solid organ to negate the effect of various pathologies on CTTA parameters. The impact of energy levels of monoenergetic images on CTTA could be addressed on large cohort future studies. Additionally, future projects could focus on identifying ideal monoenergetic image energy levels to optimize the extraction of useful biological information, similar to keV optimization studies for different imaging applications [49, 50].

## Conclusion

The energy levels of monoenergetic DECT images have a variable impact on the different CTTA parameters; certain CTTA parameters may be reliably compared between the images of different keV values such as skewness, kurtosis, and filtered mean intensity whereas mean attenuation, entropy, MPP, and SD values decrease significantly with increasing energy levels of monoenergetic images. The energy levels of monoenergetic images must be standardized and/or appropriate normalization approaches to quantification (for certain metrics) should be undertaken to ensure greater comparability of different image datasets for CTTA in oncological patients. Knowledge of these relationships can assist the understanding of results obtained from clinical CTTA studies in oncological patients undergoing DECT.

### Compliance with ethical standards

**Disclosure** Balaji Ganeshan: director, part-time employee, and shareholder of Feedback Plc (Cambridge, England, UK), company that develops and markets the TexRAD texture analysis algorithm described in this manuscript. Dushyant Sahani: GE healthcare research grant, royalties from Elsevier.

**Funding** This study was not funded.

**Ethical approval** This article does not contain any studies with human participants performed by any of the authors.

**Conflict of Interest** Balaji Ganeshan is director, part-time employee, and shareholder of Feedback Plc (Cambridge, England, UK), company that develops and markets the TexRAD texture analysis algorithm described in this manuscript. Dushyant Sahani has GE healthcare re-

search grant, royalties from Elsevier, other authors declare that they have no conflict of interest.

## References

- Gerlinger M, Rowan AJ, Horswell S, et al. (2012) Intratumor heterogeneity and branched evolution revealed by multiregion sequencing. *N Engl J Med* 366(10):883
- Davnull F, Yip CSP, Ljungqvist G, et al. (2012) Assessment of tumor heterogeneity: an emerging imaging tool for clinical practice? *Insights Imaging*. 3(6):573–589
- Ganeshan B, Miles KA (2013) Quantifying tumour heterogeneity with CT. *Cancer Imaging Off Publ Int Cancer Imaging Soc*. 26(13):140–149
- Armato SG, Li F, Giger ML, et al. (2002) Lung cancer: performance of automated lung nodule detection applied to cancers missed in a CT screening program. *Radiology*. 225(3):685–692
- Armato SG, Giger ML, MacMahon H (2001) Automated detection of lung nodules in CT scans: preliminary results. *Med Phys*. 28(8):1552–1561
- Giger ML, Bae KT, MacMahon H (1994) Computerized detection of pulmonary nodules in computed tomography images. *Invest Radiol*. 29(4):459–465
- Halligan S, Mallett S, Altman DG, et al. (2011) Incremental benefit of computer-aided detection when used as a second and concurrent reader of CT colonographic data: multiobserver study. *Radiology*. 258(2):469–476
- Lawrence EM, Pickhardt PJ, Kim DH, Robbins JB (2010) Colorectal polyps: stand-alone performance of computer-aided detection in a large asymptomatic screening population. *Radiology*. 256(3):791–798
- Li J, Van Uitert R, Yao J, et al. (2008) Wavelet method for CT colonography computer-aided polyp detection. *Med Phys*. 35(8):3527–3538
- Gletsos M, Mouggiakakou SG, Matsopoulos GK, et al. (2003) A computer-aided diagnostic system to characterize CT focal liver lesions: design and optimization of a neural network classifier. *IEEE Trans Inf Technol Biomed Publ IEEE Eng Med Biol Soc*. 7(3):153–162
- Huang Y-L, Chen J-H, Shen W-C (2006) Diagnosis of hepatic tumors with texture analysis in nonenhanced computed tomography images. *Acad Radiol*. 13(6):713–720
- Kido S, Kuriyama K, Higashiyama M, Kasugai T, Kuroda C (2002) Fractal analysis of small peripheral pulmonary nodules in thin-section CT: evaluation of the lung-nodule interfaces. *J Comput Assist Tomogr*. 26(4):573–578
- Klein HM, Klose KC, Eisele T, et al. (1993) The diagnosis of focal liver lesions by the texture analysis of dynamic computed tomograms. *ROFO Fortschr Geb Rontgenstr Nuklearmed*. 159(1):10–15
- Way TW, Sahiner B, Chan H-P, et al. (2009) Computer-aided diagnosis of pulmonary nodules on CT scans: improvement of classification performance with nodule surface features. *Med Phys*. 36(7):3086–3098
- Ganeshan B, Skogen K, Pressney I, Coutroubis D, Miles K (2012) Tumour heterogeneity in oesophageal cancer assessed by CT texture analysis: preliminary evidence of an association with tumour metabolism, stage, and survival. *Clin Radiol*. 67(2):157–164
- Ganeshan B, Abaleke S, Young RCD, Chatwin CR, Miles KA (2010) Texture analysis of non-small cell lung cancer on unenhanced computed tomography: initial evidence for a relationship with tumour glucose metabolism and stage. *Cancer Imaging Off Publ Int Cancer Imaging Soc*. 6(10):137–143
- Ganeshan B, Panayiotou E, Burnand K, Dizdarevic S, Miles K (2012) Tumour heterogeneity in non-small cell lung carcinoma assessed by CT texture analysis: a potential marker of survival. *Eur Radiol*. 22(4):796–802
- Haider MA, Vosough A, Khalvati F, et al. (2017) CT texture analysis: a potential tool for prediction of survival in patients with metastatic clear cell carcinoma treated with sunitinib. *Cancer Imaging*. 17:4
- Ng F, Ganeshan B, Kozarski R, Miles KA, Goh V (2013) Assessment of primary colorectal cancer heterogeneity by using whole-tumor texture analysis: contrast-enhanced CT texture as a biomarker of 5-year survival. *Radiology*. 266(1):177–184



20. Ozkan E, West A, Dedelow JA, et al. (2015) CT gray-level texture analysis as a quantitative imaging biomarker of epidermal growth factor receptor mutation status in adenocarcinoma of the lung. *Am J Roentgenol.* 205(5):1016–1025
21. Shac Y, Liu L, Wang F, et al. (2008) Quantitative evaluation of CT-MRI images of various tumors with expansive or infiltrative growth pattern. *Zhonghua Yi Xue Za Zhi.* 88(21):1503–1506
22. Win T, Miles KA, Janes SM, et al. (2013) Tumor heterogeneity and permeability as measured on the CT component of PET/CT predict survival in patients with non-small cell lung cancer. *Clin Cancer Res Off J Am Assoc Cancer Res.* 19(13):3591–3599
23. Hayano K, Tian F, Kambadakone AR, et al. (2015) Texture analysis of non-contrast enhanced CT for assessing angiogenesis and survival of soft tissue sarcoma. *J Comput Assist Tomogr.* 39(4):607–612
24. Goh V, Ganeshan B, Nathan P, et al. (2011) Assessment of response to tyrosine kinase inhibitors in metastatic renal cell cancer: CT texture as a predictive biomarker. *Radiology.* 261(1):165–171
25. Ahn SJ, Kim JH, Park SJ, Han JK (2016) Prediction of the therapeutic response after FOLFOX and FOLFIRI treatment for patients with liver metastasis from colorectal cancer using computerized CT texture analysis. *Eur J Radiol.* 85(10):1867–1874
26. De Cecco CN, Ganeshan B, Ciolina M, et al. (2015) Texture analysis as imaging biomarker of tumoral response to neoadjuvant chemoradiotherapy in rectal cancer patients studied with 3-T magnetic resonance. *Invest Radiol.* 50(4):239–245
27. Rao S-X, Lambregts DM, Schnerr RS, et al. (2016) CT texture analysis in colorectal liver metastases: A better way than size and volume measurements to assess response to chemotherapy? *United Eur Gastroenterol J.* 4(2):257–263
28. Ravanelli M, Farina D, Morassi M, et al. (2013) Texture analysis of advanced non-small cell lung cancer (NSCLC) on contrast-enhanced computed tomography: prediction of the response to the first-line chemotherapy. *Eur Radiol.* 23(12):3450–3455
29. Yip SSF, Coroller TP, Sanford NN, et al. (2016) Use of registration-based contour propagation in texture analysis for esophageal cancer pathologic response prediction. *Phys Med Biol.* 61(2):906–922
30. Tian F, Hayano K, Kambadakone AR, Sahani DV (2015) Response assessment to neoadjuvant therapy in soft tissue sarcomas: using CT texture analysis in comparison to tumor size, density, and perfusion. *Abdom Imaging.* 40(6):1705–1712
31. Wu J, Gong G, Cui Y, Li R (2016) Intratumor partitioning and texture analysis of dynamic contrast-enhanced (DCE)-MRI identifies relevant tumor subregions to predict pathological response of breast cancer to neoadjuvant chemotherapy. *J Magn Reson Imaging JMRI.* 44(5):1107–1115
32. Teruel JR, Heldahl MG, Goa PE, et al. (2014) Dynamic contrast-enhanced MRI texture analysis for pretreatment prediction of clinical and pathological response to neoadjuvant chemotherapy in patients with locally advanced breast cancer. *NMR Biomed.* 27(8):887–896
33. Michoux N, Van den Broeck S, Lacoste L, et al. (2015) Texture analysis on MR images helps predicting non-response to NAC in breast cancer. *BMC Cancer.* 5(15):574
34. Ahmed A, Gibbs P, Pickles M, Turnbull L (2013) Texture analysis in assessment and prediction of chemotherapy response in breast cancer. *J Magn Reson Imaging JMRI.* 38(1):89–101
35. Parakh A, Baliyan V, Sahani DV (2017) Dual-energy CT in focal and diffuse liver disease. *Curr Radiol Rep.* 5(8):35
36. Parakh A, Patino M, Sahani DV. Spectral CT/dual-energy CT. In Springer Berlin Heidelberg; 2017 [cited 2017 Apr 3]. p. 1–21. (Medical Radiology). [http://link.springer.com.ezp-prod1.hul.harvard.edu/chapter/10.1007/174\\_2017\\_28](http://link.springer.com.ezp-prod1.hul.harvard.edu/chapter/10.1007/174_2017_28)
37. Patel BN, Alexander L, Allen B, et al. (2017) Dual-energy CT workflow: multi-institutional consensus on standardization of abdominopelvic MDCT protocols. *Abdom Radiol.* 42(3):676–687
38. Mileto A, Barina A, Marin D, et al. (2015) Virtual monochromatic images from dual-energy multidetector CT: variance in CT numbers from the same lesion between single-source projection-based and dual-source image-based implementations. *Radiology.* 279(1):269–277
39. Ganeshan B, Goh V, Mandeville HC, et al. (2013) Non-small cell lung cancer: histopathologic correlates for texture parameters at CT. *Radiology.* 266(1):326–336
40. Miles KA, Ganeshan B, Hayball MP (2013) CT texture analysis using the filtration-histogram method: what do the measurements mean? *Cancer Imaging Off Publ Int Cancer Imaging Soc.* 13(3):400–406
41. Hsu CC-T, Kwan GNC, Singh D, Pratap J, Watkins TW. Principles and clinical application of dual-energy computed tomography in the evaluation of cerebrovascular disease. *J Clin Imaging Sci [Internet].* 2016 Jun 29 [cited 2017 Jun 14];6. : <http://www.ncbi.nlm.nih.gov/pmc/articles/PMC4964665/>
42. Kaza RK, Ananthakrishnan L, Kambadakone A, Platt JF (2017) Update of dual-energy CT applications in the genitourinary tract. *Am J Roentgenol.* 208(6):1185–1192
43. Roele ED, Timmer VCML, Vaassen LAA, van Kroonenburgh AMJL, Postma AA. Dual-energy CT in head and neck imaging. *Curr Radiol Rep [Internet].* 2017 [cited 2017 Jun 14];5(5). <http://www.ncbi.nlm.nih.gov/pmc/articles/PMC5371622/>
44. Liguori C, Frauenfelder G, Massaroni C, et al. (2015) Emerging clinical applications of computed tomography. *Med Devices Auckl NZ.* 5(8):265–278
45. De Cecco CN, Boll DT, Bolus DN, et al. (2017) White paper of the society of computed body tomography and magnetic resonance on dual-energy CT, part 4: abdominal and pelvic applications. *J Comput Assist Tomogr.* 41(1):8–14
46. Ganeshan B, Miles KA, Young RCD, Chatwin CR (2007) In search of biologic correlates for liver texture on portal-phase CT. *Acad Radiol.* 14(9):1058–1068
47. Ganeshan B, Miles KA, Young RCD, Chatwin CR (2009) Texture analysis in non-contrast enhanced CT: impact of malignancy on texture in apparently disease-free areas of the liver. *Eur J Radiol.* 70(1):101–110
48. Miles KA, Ganeshan B, Griffiths MR, Young RCD, Chatwin CR (2009) Colorectal cancer: texture analysis of portal phase hepatic CT images as a potential marker of survival. *Radiology.* 250(2):444–452
49. Agrawal MD, Pinho DF, Kulkarni NM, et al. (2014) Oncologic applications of dual-energy CT in the abdomen. *RadioGraphics.* 34(3):589–612
50. Yu L, Leng S, McCollough CH (2012) Dual-energy CT-based monochromatic imaging. *AJR Am J Roentgenol.* 199(5 Suppl):S9–S15